ARTICLE   OPEN

Rationalizing and engineering Rashba spin-splitting in ferroelectric oxides

Hania Djani[1,2], Andres Camilo Garcia-Castro[2,3], Wen-Yi Tong[2], Paolo Barone[4], Eric Bousquet[2], Silvia Picozzi[4] and Philippe Ghosez[2]

Ferroelectric Rashba semiconductors (FERSC), in which Rashba spin-splitting can be controlled and reversed by an electric field, have recently emerged as a new class of functional materials useful for spintronic applications. The development of concrete devices based on such materials is, however, still hampered by the lack of robust FERSC compounds. Here, we show that the coexistence of large spontaneous polarization and sizeable spin–orbit coupling is not sufficient to have strong Rashba effects and clarify why simple ferroelectric oxide perovskites with transition metal at the B-site are typically not suitable FERSC candidates. By rationalizing how this limitation can be by-passed through band engineering of the electronic structure in layered perovskites, we identify the Bi_2WO_6 Aurivillius crystal as a robust ferroelectric with large and reversible Rashba spin-splitting, that can even be substantially doped without losing its ferroelectric properties. Importantly, we highlight that a unidirectional spin–orbit field arises in layered Bi_2WO_6, resulting in a protection against spin-decoherence.

INTRODUCTION

In non-magnetic solids, one can naively expect the energy bands of electrons of up and down spins to be degenerate in absence of magnetic fields. However, in systems that break spatial inversion symmetry, e.g., at surfaces and interfaces but also in non-centrosymmetric bulk crystals, spin–orbit coupling (SOC) can lift such spin band degeneracy through the so-called Rashba and Dresselhaus effects.[1–3] During the last decade, these phenomena have attracted increasing interests in various fields, including spintronics, quantum computing, topological matter, and cold atom systems.[4,5]

Recently, the concept of ferroelectric Rashba semiconductors (FERSC) has been introduced.[6] It defines a new class of functional materials combining ferroelectric and Rashba effects, in which the spin-texture related to the Rashba spin-splitting (RSS) can be electrically switched upon reversal of the ferroelectric polarization. As such, FERSC offer exciting perspectives for spintronic applications. The Rashba spin precession of a current injected in such materials can be controlled in a non-volatile way by their reversible ferroelectric polarization. Moreover, FERSC allow to envision new devices interconverting electron- and spin-currents based on the Edelstein[7] and reverse-Edelstein[8] effects. In two-dimensional ferroelectric materials with in-plane polarization and strong anisotropy in the electronic structure, the spin–orbit field (SOF) was also proposed to have unidirectional out-of-plane alignment: $\vec{\Omega}_{SOF}(\vec{k}) = \alpha(\vec{P} \times \vec{k}) = \alpha k_y \hat{z}$, where α is a system-dependent coefficient.[9] In such a case, injected electrons with in-plane spins would therefore precess around the $\vec{z}$ axis, giving rise to a long-lived persistent spin helix (PSH), a concept originally proposed for quantum-wells of III–V semiconductors with fine-tuned Dresselhaus and Rashba coefficients[10–15] and very recently extended to a subclass of non-centrosymmetric bulk materials.[16] Independently, FERSC can also, in some cases, exhibit ferro-valley properties.[17]

The basic idea of FERSC was first put forward theoretically in bulk GeTe[18] and then experimentally confirmed in GeTe thin films.[18–20] Unfortunately, GeTe does not appear as the best candidate for concrete applications, due to its very small bandgap and related large leakage currents that, in most cases, prevent polarization switching.[6] The identification of alternative robust FERSC is therefore mandatory to achieve full exploitation of the concept. Although different directions have been explored,[21–28] no really convincing candidate has emerged yet.

Here, we rationalize by means of first-principles approaches the discovery of a promising FERSC in the family of oxide perovskite compounds. Focusing first on simple perovskites, we highlight that robust ferroelectricity and SOC are necessary but not sufficient conditions to get an efficient FERSC. Furthermore, we clarify why these materials are typically not suitable candidates. We then propose a strategy to by-pass their intrinsic limitation in layered perovskites and identify the Bi_2WO_6 Aurivillius phase as the first robust ferroelectric with large and reversible Rashba spin-splitting at the bottom of the conduction band and unidirectional SOF. We finally show that a significant n-type doping does not lead to a loss of its ferroelectric properties, suggesting the possibility of creating a doped FERSC appropriate for practical applications.

[1]Centre de Développement des Technologies Avancées, cité 20 août 1956, B.P. 17, Baba Hassen, Alger, Algeria; [2]Theoretical Materials Physics, Q-MAT, CESAM, Université de Liège, B-4000 Liège, Belgium; [3]Escuela de Física, CIMBIOS Research Group, Universidad Industrial de Santander, Cra. 27 Cll. 9, Bucaramanga, Colombia and [4]Consiglio Nazionale delle Ricerche (CNR-SPIN) c/o Univ. "G. D'Annunzio", Chieti, Italy
Correspondence: Hania Djani (hdjani@cdta.dz) or Andres Camilo Garcia-Castro (acgarcia@uis.edu.co) or Philippe Ghosez (philippe.ghosez@uliege.be)
These authors contributed equally: Hania Djani, Andres Camilo Garcia-Castro
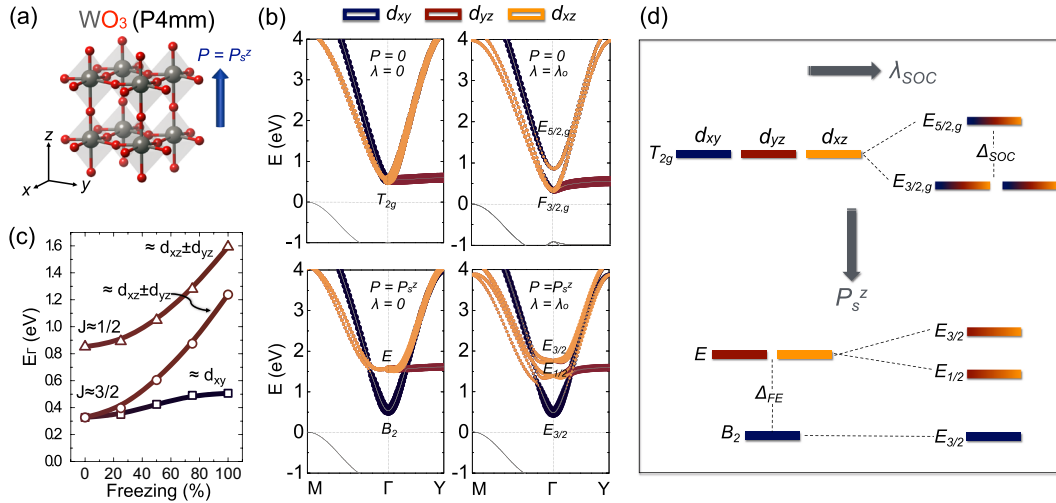
Fig. 1 Electronic dispersion curves in the *P4mm* phase of WO_3. **a** Sketch of the *P4mm* phase of WO_3, with P_s along the z-axis. **b** Evolution of the electronic band structure around the Fermi level when activating the polar distortion ($P = 0 \rightarrow P_s^z$) and SOC ($\lambda = 0 \rightarrow \lambda_0$). Projection on the t_{2g} orbitals (d_{xy}, d_{yz}, d_{zx}) of the reference structure ($P = 0$, $\lambda = 0$) are highlighted in colors. **c** Evolution of the splitting of the original t_{2g} states at Γ-point for increasing polar distortion ($P = 0 \rightarrow P_s^z$) when including SOC ($\lambda = \lambda_0$). The projection on the t_{2g} orbitals are highlighted by mixing colors as in panel (**b**). **d** Sketch of the level splittings at Γ produced by SOC (Δ_{SOC}) and ferroelectric distortion (Δ_{FE})

RESULTS

Simple perovskites

Ideal FERSC materials must meet a series of requirements. They should be non-magnetic ferroelectrics insulators with a sizable switchable polarization and a reasonable bandgap. They should include heavy ions with large SOC exhibiting a significant RSS close to the valence or conduction band edge, which should be reversible with the polarization and, for applications based on spin/charge currents, should survive to appropriate doping.

Regarding ferroelectricity, it is natural to look at $d^0 ABO_3$ perovskites with a transition metal at the B-site,[29] in which the bandgap is formally between O-2p and B-d states. As such, a large RSS around the bandgap would be more easily achieved by means of a heavy cation at the B-site while B-type ferroelectricity would likely favor an efficient polarization control of the RSS.

Tungsten oxide, WO_3, is in line with previous requirements. It adopts the perovskite structure with an empty A-site and a heavy W atom on the B-site (see Fig. 1a). It is also an insulator with formal d^0 occupancy of the W $5d$ states. Although not intrinsically ferroelectric—it adopts a nonpolar $P2_1/c$ ground state[30]—a recent study highlighted that it possesses low-energy metastable ferroelectric phases with large spontaneous polarizations ($P_s \approx 50 - 70$ μC·cm^{-2}) arising from the opposite motion of W and O atoms (Supplemental Material II.A).[31] Although never observed experimentally, these polar phases appear to be relevant prototypical states to investigate and rationalize the interplay between polarization and SOC in perovskite-like systems.

Figure 1a presents a sketch of the *P4mm* ferroelectric phase of WO_3, which exhibits a spontaneous polarization along the cartesian z-axis ($P_s^z = 54$ μC·cm^{-2}). In Fig. 1b, we show the calculated electronic band structure around the bandgap of the cubic and tetragonal *P4mm* phase of WO_3 with and without SOC. In the cubic phase ($P_s^z = 0$) without SOC ($\lambda = 0$), the bottom of the conduction band of WO_3 is at Γ and consists of triply degenerate state of t_{2g} symmetry (pure d_{xy}, d_{yz}, and d_{zx} orbitals). On the one hand, activating SOC ($\lambda = \lambda_0$) mixes the three t_{2g} states and produces a splitting Δ_{SOC} (Fig. 1d) between a doubly degenerate low-energy state of $F_{3/2,g}$ symmetry ($J = 3/2$) and a higher-energy state of $E_{5/2,g}$ symmetry ($J = 1/2$).[32] On the other hand, the *P4mm* phase ($P = P_s^z$) without SOC has a splitting Δ_{FE} (Fig. 1d) between a low-energy state of B_2 symmetry (pure d_{xy}

orbital perpendicular to P_s^z at first perturbative order) and a higher-energy doubly degenerate state of E symmetry (mixed d_{yz} and d_{zx} orbitals, partly hybridized with O 2p).[33] In the presence of both SOC and ferroelectric polarization, three distinct levels of $E_{3/2}$, $E_{1/2}$ and $E_{3/2}$ symmetry are present. For small amplitude of P_s^z, Δ_{FE} is small compared with Δ_{SOC} and all the three levels arise from a mixing of the three t_{2g} orbitals (see Fig. 1c). As P_s^z and Δ_{FE} increase, the lowest $E_{3/2}$ acquires a dominant d_{xy} character (like the B_2 state without SOC) while the higher-energy $E_{1/2}$ and $E_{3/2}$ levels are a mixing of d_{yz} and d_{zx} orbitals. This is supported by a simple tight-binding model (see Supplemental Material II.B).

Estimate of the RSS strength in the *P4mm* phase through the effective Rashba parameter $a_R = 2E_R/k_R$[34,35] (see Supplemental Material I) gives a sizable value $a_R \approx 0.7$ eV·Å for the upper bands linked to $E_{3/2}$ and $E_{1/2}$ states. However, $a_R \approx 0$ for the band linked to the lowest $E_{1/2}$ state with strongly dominant d_{xy} character (d_{xy} is perpendicular to P_s^z).

The same conclusions apply to the ferroelectric *Amm*2 phase of WO_3 (see Fig. 2 and Supplemental Material II.C) where the polarization is along the xy pseudo-cubic direction (x' in a reference axis rotated by 45° around z with respect to x) and with a calculated $P_s^{x'} = 69$ μC cm^{-2}. In this orthorhombic phase, the reference t_{2g} states are split in three levels of $E_{1/2}$ symmetry. The lowest state has a strongly dominant $d_{y'z}$ character ($d_{y'z}$ is perpendicular to $P_s^{x'}$) and does not show any significant RSS.

These results are in fact generic to ABO_3 perovskites and remain valid in presence of a ("non-empty") A-cation, as in $KTaO_3$ (see ref. [36] and Supplemental Material III): the first unoccupied d-band is related to the orbital perpendicular to P_s ($d_\perp$) and does not show significant RSS in the presence of ferroelectric polarization.

A natural question at this stage is why the lowest t_{2g} state does not show RSS. As highlighted from a simple tight-binding model restricted to the t_{2g} subspace (see Supplemental Material II.B.1), all the three levels are allowed to show RSS but $a_R \propto \Delta_{SOC}/\Delta_{FE}$ and should vanish for all states in the limit of large Δ_{FE}. The question is then rather why the upper t_{2g} states show significant RSS. A plausible explanation is their interactions with the 2p states of bridging oxygen atoms. Combining an extended tight-binding model and first-principles calculations, we instead identify that the dominant effect comes actually from their hybridization with the e_g states (see Supplemental Material II.B.2-3).
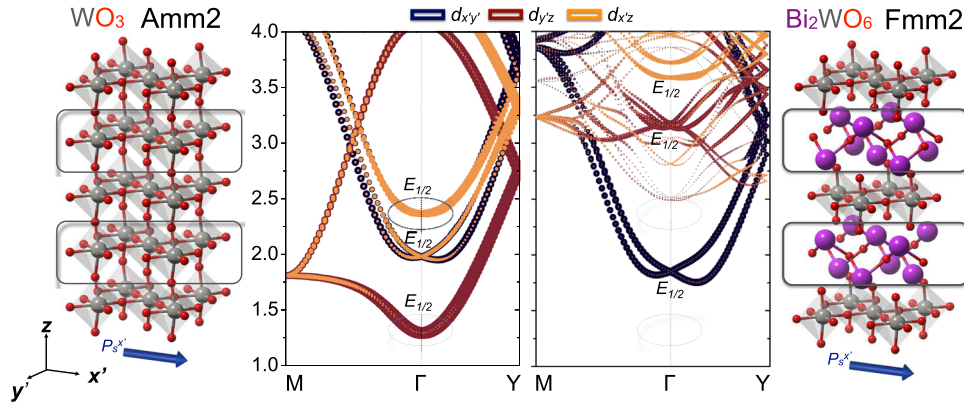
Fig. 2 Comparison of WO_3 and Bi_2WO_6. Sketch of the atomic structure and electronic dispersion along the Γ–Y direction focusing on the lowest conduction states, $E_F = 0$) of the Amm2 phase of WO_3 (left) and Fmm2 phase of Bi_2WO_6 (right). Contribution of the t_{2g} orbitals (d_{xy}, d_{yz}, d_{zx}) to the different electronic states are highlighted in colors

This rationalizes that significant RSS can appear in the t_{2g} conduction states of $d^0 ABO_3$ perovskites with heavy B-site atoms. However, RSS is restricted to the upper t_{2g} levels showing significant hybridization with the e_g states. Consequently, achieving a large a_R at the conduction band bottom of perovskites would require to get rid of the lowest energy state associated with the $d_\perp$ orbital perpendicular to P_s. As we now show, this can be achieved if one confines the ferroelectric material in the direction perpendicular to P_s, which is naturally realized for WO_3 in the $Bi_2W_nO_{3n+3}$ Aurivillius series, a family of single-phase layered compounds alternating WO_3 perovskite blocks with Bi_2O_2 fluorite-like layers.

Layered perovskites

Bi_2WO_6 is the $n = 1$ member of the $Bi_2W_nO_{3n+3}$ series. It is a strong ferroelectric with large polarization ($P_s \approx 50 \mu C\, cm^{-2}$ [37], see Supplemental Material IV.A), and high Curie temperature ($T_c = 950\,°C$ [38]). It has a measured experimental gap of 2.7–2.8 eV [39,40] defined between the O 2p and W 5d states of the perovskite block (see Supplemental Material IV.B). Furthermore, Bi_2WO_6 is prone to n-type doping.[37,41]

Bi_2WO_6 exhibits a polar orthorhombic $P2_1ab$ phase up to 670 °C, at which it undergoes a phase transition to another polar orthorhombic phase of $B2cb$ symmetry, stable up to 950 °C.[38,42] As discussed in ref. [42], the polar $B2cb$ and $P2_1ab$ phases are small distortions of the same reference $I4/mmm$ high-symmetry structure and arise from the consecutive condensation of independent atomic motions: (i) a polar distortion along the x'-axis (Γ_5^- symmetry) lowering the symmetry from $I4/mmm$ to $Fmm2$, (ii) tilts of the oxygen octahedra along the x'-axis (X_3^+ symmetry) lowering further the symmetry to $B2cb$ and (iii) rotations of the oxygen octahedra around the z-axis (X_2^+ symmetry) bringing the system in its $P2_1ab$ ground state.

The polar $Fmm2$ phase of Bi_2WO_6 is comparable to the $Amm2$ phase of bulk WO_3 (Fig. 2) with a spontaneous polarization $P_s^{x'}$ in the xy pseudo-cubic directions and oriented in plane (i.e., perpendicular to the stacking direction). In Fig. 2, we compare the electronic band structure of $Amm2$ WO_3 and $Fmm2$ Bi_2WO_6 in the presence of SOC. In both cases, the t_{2g} states at Γ are split into 3 distinct $E_{1/2}$ levels. However, in Bi_2WO_6 due to the asymmetry imposed by the Bi_2O_2 layers along the z-axis, the states associated to the W $d_{x'z}$ and $d_{y'z}$ orbitals are pushed to much higher energy than the $d_{x'y'}$. Consequently, the $E_{1/2}$ level at the conduction band bottom is now the one with dominant $d_{x'y'}$ character and it exhibits a large a_R of 1.28 eV·Å.

Since the $Fmm2$ phase is not observed experimentally, we now analyze how oxygen-octahedra rotations (X_3^+ and X_2^+) present in the $B2cb$ and $P2_1ab$ phase on top of the polar distortions (Γ_5^-) affect the

Table 1. Computed spontaneous polarization (P_s), k-vector splitting (k_R), energy splitting (E_R), Rashba parameter (a_R), and energy gap (E_g) for distinct ferroelectric phases of Bi_2WO_6. Values in few selected reference systems are reported for comparison

		P_s ($\mu C\cdot cm^{-2}$)	k_R ($Å^{-1}$)	E_R (meV)	a_R (eV·Å)	E_g (eV)
Bi_2WO_6	$Fmm2$	78	0.155	99.4	1.28	1.82
	$B2cb$	67	0.136	53.0	0.78	1.77
	$B2cm$	68	0.168	101.9	1.22	1.94
	$P2_1ab$	65	0.163	71.4	0.88	1.83
$BiAlO_3$[21]	$R3c$	79	0.04	7	0.39	2.57
$GeTe$[18]	$R3m$	60	0.09	227	4.80	0.38
$BiTeI$[35]	$P3m1$	–	0.052	100	3.85	0.43

RSS. In order to clarify the independent role of X_3^+ and X_2^+ distortions, we compare, in Table 1, a_R in distinct fully relaxed ferroelectric phases: $Fmm2$ (Γ_5^-), $B2cb$ ($\Gamma_5^- + X_3^+$), $B2cm$ ($\Gamma_5^- + X_2^+$), and $P2_1ab$ ($\Gamma_5^- + X_3^+ + X_2^+$). It appears that the RSS is dominantly produced by the polar Γ_5^- distortion, while oxygen rotations play a detrimental but much minor role (see Supplemental Material IV.C): the X_3^+ distortion tends to decrease a_R, while the X_2^+ distortion has no direct effect. In fact k_R stays almost unchanged in all the phases, while E_R is more affected. Overall, the amplitude of a_R in the $P2_1ab$ ground state is slightly reduced but remains comparable to that of the $Fmm2$ phase.

Figure 3a shows the electronic dispersion curves of the $P2_1ab$ phase, highlighting the significant spin-splitting at the conduction band bottom. We notice an additional band splitting due to the presence of the oxygen tilts (X_3^+ distortion) that doubles the unit cell in the $y'z$-plane. Constant energy maps are also shown for an energy of 2.0 eV, along with the corresponding spin-texture. The relative orientation of the coupled k and S components is determined by the symmetry of the system; in our case, the four polar phases belong to the C_{2v} point group that contains a C_{2x} twofold rotation around the polar x'-axis and two mirror planes, $m_{\perp y}$ and $m_{\perp z}$. The electronic structure has the shape of two partially overlapping revolution paraboloids with revolution axes symmetrically shifted in opposite directions with respect to $k_y = 0$. These two paraboloids are associated to electrons with opposite S_z spin component and an additional S_y contribution ensuring rotation of S in the region where the ellipsoids cross. No S_x component is observed, consistently with the Rashba-like effect. The RSS is proportional to the polarization and is reversed under polarization switching (Fig. 3b).
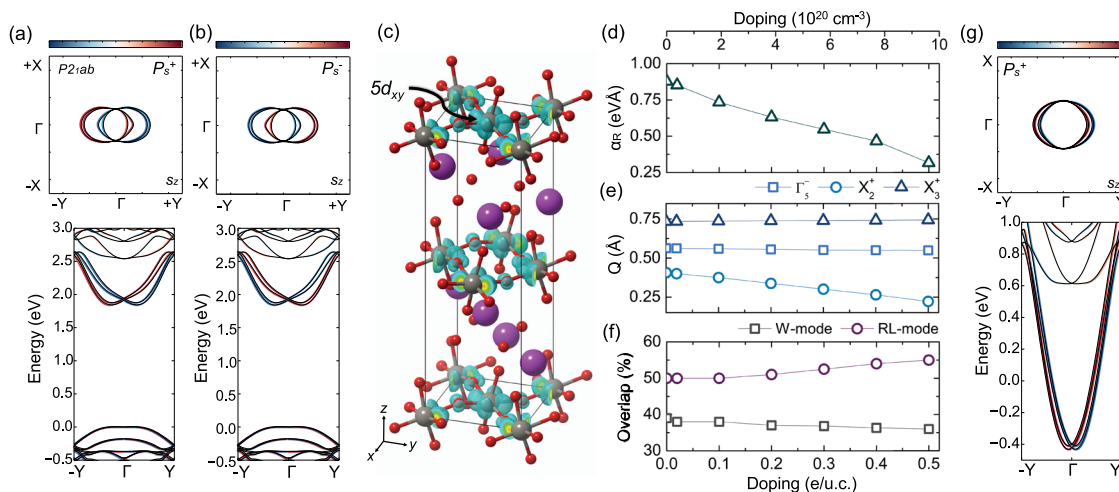
Fig. 3 Pristine and n-doped $P2_1ab$ phase of Bi_2WO_6. **a, b** S_z spin-projected band dispersion around the Fermi level (bottom) and spin-texture into k_xk_y plane at $E = 2.0$ eV (top) of pristine Bi_2WO_6 in its $P2_1ab$ phase for **a** up and **b** down polarization directions. A reversible spin-splitting is observed at the conduction band bottom. **c** Charge-density of the conduction bands in the $P2_1ab$ phase of Bi_2WO_6 with a doping of 0.5 e/u.c. **d–f** Evolution with the electronic doping concentration of, respectively, **d** the Rashba parameter, **e** the Γ_5^-, X_2^+, and X_3^+ distortion amplitudes, and **f** the respective W-mode and RL-mode contributions to Γ_5^- distortion in the $P2_1ab$ phase of Bi_2WO_6. **g** S_z spin-projected bands (bottom) and spin-texture into k_xk_y plane at $E_F = 0$ eV (top) in the $P2_1ab$ phase of Bi_2WO_6 with a doping of 0.5 e/u.c. A characteristic 2DEG-like behavior is observed from the parabolic band shape

It can also be noted that the spin-splitting vanishes along the $\Gamma \rightarrow X$ path, corresponding to the polarization direction. As such, all the symmetry constraints and design criteria proposed in refs. [9,16] in order to have a unidirectional SOF are met. Specifically, the crystal symmetries impose that such unidirectional SOF is preserved even when including higher-order spin-momentum coupling terms, thus ruling out spin-decoherence effects based on the Dyakonov-Perel relaxation mechanism.[11,12] We therefore conjecture the spin-lifetime in Bi_2WO_6 to be long, possibly leading to a long-lived and nanometer-sized persistent spin helix,[10–15] which could be of high relevance for future spintronic applications.

Doping

So far, we have shown Bi_2WO_6 to be a robust switchable ferroelectric with large reversible RSS at the conduction band bottom making it already a promising candidate for FERSC optical devices. To be also of practical utility for spintronic applications based on charge/spin-currents, it should additionally be possible to dope it with electrons, which contrary to some other Aurivillius, appears to be naturally the case.[37,41] Moreover, it should keep its FERSC properties when n-doped. This is far from obvious, since adding conduction electrons is expected to suppress ferroelectricity (and related RSS). Nevertheless, recent studies have shown that prototypical ferroelectrics like $BaTiO_3$ can preserve their ferroelectric distortion under n-doping concentrations up to 0.1 e/u.c.[43,44]

In Fig. 3, we report the evolution of structural and electronic properties of the $P2_1ab$ phase of Bi_2WO_6 under electron doping (see Methods). In line with the electronic structure of the pristine material, doping electrons occupy the W 5d states around the conduction band bottom. Due to the dominant $d_{x'y'}$ character of these states, these electrons form a two-dimensional electron gas (2DEG) confined in the perovskite layer (Fig. 3c). Amazingly, symmetry-adapted mode analysis of the atomic distortion of the doped structure with respect to the $I4/mmm$ reference structure indicates that the global Γ_5^- polar distortion remains constant under electron doping (Fig. 3e), rather than being suppressed. Further insights are given by the projection of this distortion on

the phonon eigendisplacement vectors of the $I4/mmm$ reference (in Fig. 3f). The global Γ_5^- polar distortion arises in fact from the condensation of two distinct phonon modes: a "W-mode" confined in the WO_3 layer and related to the off-centering of W in its O octahedron cage and a "RL-mode" (i.e., rigid-layer mode[42,45]), related to a nearly rigid motion of the Bi_2O_2 layer with respect to the perovskite block. Although the global polar distortion remains constant under n-doping, the contribution of the W-mode is progressively suppressed when increasing the population of the W $5d_{xy}$ states, while that of the RL-mode is amplified.

Concomitantly with the suppression of the W-mode distortion, α_R (Fig. 3b) is progressively reduced under doping, highlighting that large polar distortion is not enough to lead to large α_R; rather, the polar distortion pattern must occur around the W atom responsible for the RSS, as in the W-mode. Although progressively reduced, α_R keeps nevertheless a sizable value up to large n-doping: as illustrated in Fig. 3d, g, at a doping level of 0.5 e^-/u.c. ($\approx 10^{21}$ cm^{-3}), α_R is still as large as 0.3 eV·Å. Spin textures at intermediate carrier concentrations are reported in Supplemental Material IV.D. Such a survival of the polar distortion and related sizable RSS under significant doping is a necessary requirement for FERSC but, of course, it does not guarantee that it is still possible to achieve electric switching of the polarization, which ask for further experimental confirmation.

DISCUSSION

Combining first-principles calculations, symmetry analysis and tight-binding models, we have first rationalized step by step the RSS in the important family of ABO_3 perovskites with a transition metal at the B-site, demonstrating why they typically do not show significant RSS at the conduction band bottom. Relying on the concept of band-structure engineering in layered structures, we have then identified the Aurivillius Bi_2WO_6 compound to be the first known ferroelectric oxide to show a large Rasba-like spin-splitting at the conduction band bottom that can be reversed under polarization switching. Beyond being a practical ferroelectric, Bi_2WO_6 offers additional and appealing peculiarities with respect to previously proposed FERSC candidates: (i) a

unidirectional spin–orbit field (arising from the combined presence of in-plane polarization, strong layering-induced anisotropy in the electronic structure and related symmetry properties) that protects the spin transport from spin dephasing; (ii) the persistence of desired properties (such as robust polar distortion, large Rashba spin-splitting and unidirectional spin–orbit field) upon sizable n-doping.

A similar behavior can a priori be found in other ferroelectric Aurivillius phases, like $SrBi_2Ta_2O_9$, or even $Bi_4Ti_3O_{12}$. However, the RSS depends on the strength of the B-cation SOC that increases with the oxidation state[46] and P_s, which are maximized in W-based compounds (see Supplemental Material V). Within the $Bi_2W_nO_{3n+3}$ series, $Bi_2W_2O_9$ and $Bi_2W_3O_{12}$ show a large a_R as well (Supplemental Material V). However, $Bi_2W_2O_9$ is not ferroelectric[47] and $Bi_2W_3O_{12}$ has not been synthesized yet. Therefore, Bi_2WO_6 emerges as the best candidate so far for large RSS and unidirectional SOF in the whole family of perovskite-based oxides, calling for experimental confirmations of our theoretical predictions. Our work also motivates and rationalizes the search of alternative candidates in other families of naturally layered perovskites like Ruddlesden-Popper and Dion-Jacobson series.[48]

METHODS

First-principles calculations relied on density functional theory (DFT)[49,50] within the projected augmented waves (PAW) method[51] as implemented in the Vienna Ab initio Simulation Package (VASP).[52,53] Many results were also checked using ABINIT[54–56] with norm-conserving pseudopotentials. The exchange-correlation effects were estimated within the generalized gradient approximation (GGA) using the PBEsol parameterization.[57] The following electrons were treated as valence states: $Bi(5d^{10}6s^26p^3)$, $W(5p^6 s^25d^4)$, and $O(2s^22p^4)$. Convergence was reached using a Monkhorst-Pack[58] $8 \times 8 \times 2$ k-point mesh for Bi_2WO_6 ($8 \times 8 \times 8$ for WO_3) and a 600 eV energy cutoff. Structural relaxations were converged until forces were <1 meV·Å^{-1}. The spin–orbit coupling was included into the calculations as in ref. [59]. Electron doping was performed by adding electrons to the total electronic density and introducing a neutralizing homogeneous background charge to compensate the additional electrons, as previously done in several works;[44,60–62] electronic and atomic relaxations were carried out at fixed volume.[63] The spin-texture was analyzed using the script PyProcar,[64] the structural distortion was analyzed with AMPLIMODE[65] and the figures of atomic structures were elaborated with VESTA.[66]

DATA AVAILABILITY

All relevant data are available from the authors upon reasonable request.

AUTHOR CONTRIBUTIONS

Ph.G. conceived the study with H.D., A.C.G.C. and E.B. and supervised the work. H.D. and A.C.G.C. did the first-principles calculations and analyzed the results. P.B., S.P., W.Y.T. and Ph.G. interpreted the electronic band structures and rationalized the RSS. Ph.G. wrote the paper with H.D., A.C.G.C. from inputs of all authors. All authors discussed the results and commented on the paper.

ADDITIONAL INFORMATION

Supplementary information accompanies the paper on the *npj Quantum Materials* website (https://doi.org/10.1038/s41535-019-0190-z).

Competing interests: The authors declare no competing interests.

Publisher's note Springer Nature remains neutral with regard to jurisdictional claims in published maps and institutional affiliations.

REFERENCES

1. Dresselhaus, G. Spin-orbit coupling effects in zinc blende structures. *Phys. Rev.* **100**, 580–586 (1955).
2. Rashba, E. I. Properties of semiconductors with an extremum loop. I. Cyclotron and combinational resonance in a magnetic field perpendicular to the plane of the loop. *Sov. Phys. Solid State* **2**, 1109–1122 (1960).
3. Bychkov, Y. A. & Rashba, E. I. Oscillatory effects and the magnetic susceptibility of carriers in inversion layers. *J. Phys. C: Solid State Phys.* **17**, 33 (1984).
4. Manchon, A. et al. New perspectives for Rashba spin-orbit coupling. *Nat. Mater.* **14**, 871–882 (2015).
5. Varignon, J., Vila, L., Barthélémy, A. & Bibes, M. A new spin for oxide interfaces. *Nat. Phys.* **14**, 322 (2018a).
6. Picozzi, S. Ferroelectric Rashba semiconductors as a novel class of multifunctional materials. *Front. Phys.* **2**, 10 (2014).
7. Edelstein, V. Spin polarization of conduction electrons induced by electric current in two-dimensional asymmetric electron systems. *Solid State Commun.* **73**, 233–235 (1990).
8. Sánchez, J. C. et al. Spin-to-charge conversion using Rashba coupling at the interface between non-magnetic materials. *Nat. Commun.* **4**, 1–7 (2013).
9. Lee, H., Im, J. & Jin, H. Harnessing the giant out-of-plane Rashba effect and the nanoscale persistent spin helix via ferroelectricity in SnTe thin films. http://arxiv.org/abs/1712.06112 (2017).
10. Schliemann, J., Egues, J. C. & Loss, D. Nonballistic spin-field-effect transistor. *Phys. Rev. Lett.* **90**, 146801–146805 (2003).
11. Bernevig, B. A., Orenstein, J. & Zhang, S.-C. Exact SU(2) symmetry and persistent spin helix in a spin-orbit coupled system. *Phys. Rev. Lett.* **97**, 236601–236605 (2006).
12. Kammermeier, M., Wenk, P. & Schliemann, J. Control of spin helix symmetry in semiconductor quantum wells by crystal orientation. *Phys. Rev. Lett.* **117**, 236801–236806 (2016).
13. Koralek, J. D. et al. Emergence of the persistent spin helix in semiconductor quantum wells. *Nature* **458**, 610 (2009).
14. Walser, M. P., Reichl, C., Wegscheider, W. & Salis, G. Direct mapping of the formation of a persistent spin helix. *Nat. Phys.* **8**, 757 (2009).
15. Schliemann, J. Colloquium: Persistent spin textures in semiconductor nanostructures. *Rev. Mod. Phys.* **89**, 011001 (2017).
16. Tao, L. L. & Tsymbal, E. Y. Persistent spin texture enforced by symmetry. *Nat. Commun.* **9**, 2763 (2018).
17. Tong, W.-Y., Gong, S.-J., Wan, X. & Duan, C.-G. Concepts of ferrovalley material and anomalous valley Hall effect. *Nat. Commun.* **7**, 13612 (2016).
18. DiSante, D., Barone, P., Bertacco, R. & Picozzi, S. Electric control of the giant Rashba effect in bulk GeTe. *Adv. Mater.* **25**, 509–513 (2013).
19. Liebmann, M. et al. Giant Rashba-type spin splitting in ferroelectric GeTe(111). *Adv. Mater.* **28**, 560–565 (2016).
20. Rinaldi, C. et al. Ferroelectric control of the spin texture in GeTe. *Nano Lett.* **18**, 2751–2758 (2018).
21. daSilveira, L. G. D., Barone, P. & Picozzi, S. Rashba-Dresselhaus spin-splitting in the bulk ferroelectric oxide $BiAlO_3$. *Phys. Rev. B* **93**, 245159–245167 (2016).
22. Stroppa, A. et al. Tunable ferroelectric polarization and its interplay with spin-orbit coupling in tin iodide perovskites. *Nat. Commun.* **5**, 5900 (2014).
23. Yamauchi, K. et al. Coupling ferroelectricity with spin-valley physics in oxide-based heterostructures. *Phys. Rev. Lett.* **115**, 037602–037607 (2015).
24. Narayan, A. Class of Rashba ferroelectrics in hexagonal semiconductors. *Phys. Rev. B* **92**, 220101–220105 (2015).
25. Zhong, Z. et al. Giant switchable rashba effect in oxide heterostructures. *Adv. Mater. Interfaces* **2**, 1400445–1400450 (2015).
26. Di Sante, D. et al. Intertwined Rashba, Dirac, and Weyl fermions in hexagonal hyperferroelectrics. *Phys. Rev. Lett.* **117**, 076401–076406 (2016).
27. Zhang, H., Deng, B., Wang, W.-C. & Shi, X.-Q. Class of diatomic ferroelectrics with multifunctional properties: IV–VI compounds in the distorted NiAs-type structure. *Phys. Rev. B* **96**, 245136–245142 (2017).
28. Varignon, J., Santamaria, J. & Bibes, M. Switchable and tunable Rashba-type soin slitting in covalent perovskite oxides. *Phys. Rev. Lett.* **122**, 116401 (2019).
29. Hill, N. A. Why are there so few magnetic ferroelectrics? *J. Phys. Chem. B* **104**, 6694–6709 (2000).
30. Salje, E. The orthorhombic phase of WO_3. *Acta Crystallogr. Sect. B* **33**, 574–577 (1977).
31. Hamdi, H., Salje, E. K. H., Ghosez, P. & Bousquet, E. First-principles reinvestigation of bulk WO_3. *Phys. Rev. B* **94**, 245124 (2016).
32. Goodenough, J. B. Spin-orbit-coupling effects in transition-metal compounds. *Phys. Rev.* **171**, 466–479 (1968).

33. Wolfram, T. & Ellialtioglu, S. *Electronic and Optical Properties of d-Band Perovskites*. 1st edn, 1–315. (Cambridge University Press, Cambridge, 2006).

34. Winkler, R. *Spin Orbit Coupling Effects in Two-Dimensional Electron and Hole Systems*. 1st edn, Vol. 191, 1–228. (Springer, Berlin Heidelberg, Berlin, 2003).

35. Ishizaka, K. et al. Giant Rashba-type spin splitting in bulk BiTeI. *Nat. Mater.* **10**, 521–526 (2011).

36. Tao, L. L. & Wang, J. Strain-tunable ferroelectricity and its control of Rashba effect in KTaO3. *J. Appl. Phys.* **120**, 1–6 (2016).

37. Noguchi, Y., Murata, K. & Miyayama, M. Defect control for polarization switching in Bi2WO6-based single crystals. *Appl. Phys. Lett.* **89**, 242916 (2006).

38. McDowell, N. A., Knight, K. S. & Lightfoot, P. Unusual high-temperature structural behaviour in ferroelectric Bi_2WO_6. *Chem.: A Eur. J.* **12**, 1493–1499 (2006).

39. Zhou, Y. et al. Monolayered Bi_2WO_6 nanosheets mimicking heterojunction interface with open surfaces for photocatalysis. *Nat. Commun.* **6**, 8340 (2015).

40. Lv, Y., Yao, W., Zong, R. & Zhu, Y. Fabrication of wide range visible photocatalyst Bi_2WO_2 nanoplates via surface oxygen vacancies. *Sci. Rep.* **6**, 19347 (2016).

41. Noguchi, Y., Murata, K. & Miyayama, M. Effects of defect control on the polarization properties in Bi_2WO_6-based single crystals. *Ferroelectrics* **355**, 55 (2007).

42. Djani, H., Bousquet, E., Kellou, A. & Ghosez, P. First-principles study of the ferroelectric Aurivillius phase Bi_2WO_2. *Phys. Rev. B* **86**, 054107–054119 (2012).

43. Kolodiazhnyi, T. et al. Persistence of ferroelectricity in $BaTiO_3$ through the insulator-metal transition. *Phys. Rev. Lett.* **104**, 147602–147606 (2010).

44. Wang, Y. et al. Ferroelectric instability under screened coulomb interactions. *Phys. Rev. Lett.* **109**, 247601–247606 (2012).

45. Machado, R., Stachiotti, M. G., Migoni, R. L. & Tera, A. H. First-principles determination of ferroelectric instabilities in Aurivillius compounds. *Phys. Rev. B* **70**, 214112–214120 (2004).

46. Dai, D., Xiang, H. & Whangbo, M.-H. Effects of spin-orbit coupling on magnetic properties of discrete and extended magnetic systems. *J. Computational Chem.* **29**, 2187–2209 (2008).

47. Champarnaud-Mesjard, J.-C., Frit, B. & Watanabe, A. Crystal structure of $Bi_2W_2O_9$, the $n=2$ member of the homologous series $(Bi_2O_2)B^{VI}_nO_{3n+1}$ of cation-deficient Aurivillius phases. *J. Mater. Chem.* **9**, 1319–1322 (1999).

48. Benedek, N. A. et al. Understanding ferroelectricity in layered perovskites: new ideas and insights from theory and experiments. *Dalton Trans.* **44**, 10543–10558 (2015).

49. Hohenberg, P. & Kohn, W. Inhomogeneous electron Gas. *Phys. Rev.* **136**, B864–B871 (1964).

50. Kohn, W. & Sham, L. J. Self-consistent equations including exchange and correlation effects. *Phys. Rev.* **140**, A1133–A1138 (1965).

51. Blöchl, P. E. Projector augmented-wave method. *Phys. Rev. B* **50**, 17953–17979 (1994).

52. Kresse, G. & Furthmüller, J. Efficient iterative schemes for ab initio total-energy calculations using a plane-wave basis set. *Phys. Rev. B* **54**, 11169–11186 (1996).

53. Kresse, G. & Joubert, D. From ultrasoft pseudopotentials to the projector augmented-wave method. *Phys. Rev. B* **59**, 1758–1775 (1999).

54. Gonze, X. et al. First-principles computation of material properties: the {ABINIT} software project. *Computational Mater. Sci.* **25**, 478–492 (2002).

55. Gonze, X. et al. A brief introduction to the ABINIT software package. *Z. f.ür. Kristallographie* **220**, 558–562 (2005).

56. Gonze, X. et al. ABINIT: first-principles approach to material and nanosystem properties. *Computer Phys. Commun.* **180**, 2582–2615 (2009).

57. Perdew, J. P. et al. Restoring the density-gradient expansion for exchange in solids and surfaces. *Phys. Rev. Lett.* **100**, 136406–136410 (2008).

58. Monkhorst, H. J. & Pack, J. D. Special points for Brillouin-zone integrations. *Phys. Rev. B* **13**, 5188–5192 (1976).

59. Hobbs, D., Kresse, G. & Hafner, J. Fully unconstrained noncollinear magnetism within the projector augmented-wave method. *Phys. Rev. B* **62**, 11556–11570 (2000).

60. Zhao, H. J. et al. Meta-screening and permanence of polar distortion in metallized ferroelectrics. *Phys. Rev. B* **97**, 054107–054118 (2018).

61. Benedek, N. A. & Birol, T. Ferroelectric metals reexamined: fundamental mechanisms and design considerations for new materials. *J. Mater. Chem. C.* **4**, 4000–4015 (2016).

62. Iwazaki, Y., Suzuki, T., Mizuno, Y. & Tsuneyuki, S. Doping-induced phase transitions in ferroelectric $BaTiO_3$ from first-principles calculations. *Phys. Rev. B* **86**, 214103–214109 (2012).

63. Bruneval, F., Varvenne, C., Crocombette, J.-P. & Clouet, E. Pressure, relaxation volume, and elastic interactions in charged simulation cells. *Phys. Rev. B* **91**, 024107–024115 (2015).

64. Romero, A. H. & Munoz, F. PyProcar (2015).

65. Orobengoa, D., Capillas, C., Aroyo, M. I. & Perez-Mato, J. M. AMPLIMODES: symmetry-mode analysis on the Bilbao Crystallographic Server. *J. Appl. Crystallogr.* **42**, 820–833 (2009).

66. Momma, K. & Izumi, F. VESTA for three-dimensional visualization of crystal, volumetric and morphology data. *J. Appl. Crystallogr.* **44**, 1272–1276 (2011).